

Visual Tracking of Biopsy Needles in 2D Ultrasound Images

Mert Kaya, Enes Senel, Awais Ahmad, and Ozkan Bebek

Abstract—Ultrasound (US) is one the most commonly used medical imaging techniques in percutaneous needle procedures. However, US images are inherently noisy and contain excessive number of artifacts. Hence, it is not easy to track the needle tip in the US images during the needle insertions. At this point, image based visual tracking techniques can be used for needle tip tracking. This paper presents a method for visual tracking of biopsy needles in 2D US images using sum of squared differences and sum of conditional variances. Second order Gauss-Newton optimization is used to decrease processing time and make the tracking more robust. The needle template images used in the method are updated with a strategy to prevent needle loss and detection failures during tracking. The paper also explains how to identify needle losses during tracking and how to recover the needle position without using a needle localization algorithm. We demonstrate the precision of the visual needle tip tracking method with experiments under challenging tracking conditions.

I. INTRODUCTION

Percutaneous needle procedures, such as biopsy and drug delivery are frequently performed medical operations. The needles can be inserted manually or with robotic assistance. During the needle insertion, tracking the needle tip is important for the success of the operations. If the needle tip is not tracked, samples can be taken from healthy tissues, or drugs can be administered to inappropriate points. Also, unwanted side effects like organ damage or hemorrhage can occur. The needle trajectory can be preplanned using needle insertion robots and the needle can be inserted with high accuracy, hence unwanted side effects can be minimized. For the success of the operations, the needle tip must be tracked using a medical imaging device.

Magnetic resonance imaging (MRI) provides clear images of anatomical structures and the needles in human body. However, non-magnetic needles must be used and workspace of the MRI is limited. The needles can be also clearly distinguished in computer tomography (CT) and fluoroscopy images but they are harmful for both patients and operators due to radiation. In addition, the workspace of CT is limited like MRI. On the other hand, ultrasound (US) does not have any known side effects and provides larger workspace. The needles can be imaged in the body with a small sized probe.

This work was supported by the Scientific and Technical Research Council of Turkey (TUBITAK) under Grant No. 112E312.

Mert Kaya and Awais Ahmad are with Department of Electrical and Electronics Engineering, Ozyegin University, Istanbul, Turkey. e-mail: mert.kaya@ozyegin.edu.tr; awais.ahmad@ozu.edu.tr

Enes Senel is with the Department of Computer Science, Ozyegin University, Istanbul, Turkey. e-mail: enes.senel@ozu.edu.tr

Ozkan Bebek is with the Department of Mechanical Engineering, Ozyegin University, Istanbul, Turkey. e-mail: ozkan.bebek@ozyegin.edu.tr

Hence, US imaging is commonly used to track the needle tip. However, the image quality is so low that tracking the needle tip can be challenging. At this point, image based tracking methods can be used to track the needle tip. A robot can guide the US probe to collect images during operation [1]. The robot assisted US probe on the patient can produce tissue deformation, which might cause the imaging plane to shift, and could result in failure to track the needle tip.

US probe provides images if the probe is in continuous contact with the tissue, since the ultrasound waves require a liquid medium to propagate. Also, needle localization algorithms are developed to work if the needle is imaged without any disruptions. During imaging, if the probe is removed and put back, misalignment between the needle axis and US imaging plane can occur. In such situations, the needle tip cannot be detected or anatomical structures can be detected as the needle tip until the US probe and needle is realigned. In order to prevent false needle detections, and recover the needle tip location correctly after the probe has contacted the tissue, the needle tip should be visually tracked.

In the literature, there are many studies conducted on tracking the needle tip in the US images. The following summarizes the studies conducted on developing the needle tip tracking algorithms. Zhao *et al.* [2] used Frangi's vesselness filter to segment the needle pixels and used the Kalman filter to track the needle tip in 3D US images. Novotny *et al.* [3] used the passive markers to track the surgical tools in 3D US images. Using appearance of passive markers in the images, they extracted position and orientation of the tools from 3D US images. Also, the tracking algorithm was implemented on a GPU for real-time tracking. Adebar *et al.* [4] localized and tracked the needle tip in 3D color US doppler using piezoelectric buzzer.

Vrooijink *et al.* [5] developed a 2D US image guided biopsy robot. The needle was localized in 3D with transverse 2D US images. The needle was inserted with a motorized system and the US probe was servoed along the needle tip. Also, needle insertion mechanism provided position feedback to localize the needle tip. Chatelain *et al.* [6] localized and tracked the needles in 3D US images. They used the volumetric frame differences to detect the needle insertion. After the insertion was detected, the US images were binarized using predefined thresholding value and the needles were localized with RANSAC algorithm. The Kalman filter was used to track the needle tip. Also, they used a 6-DOF robotic arm for servoing the 3D US probe along needle tip. Chatelain *et al.* [7] developed a robotic system for 3D US guided needle steering. They tracked the needle pixels with Bayesian tracking framework. The needles were automatically inserted

and the 3D US probe was servoed using two 6-DOF robotic arms.

In our previous studies, Gabor filter was used to segment the needle pixels and the needle axis was localized using RANSAC line fitting in [8]. Gabor filtered needle pixels were automatically binarized and the needle tip was estimated using a probability mapping method [9]. The needle tip estimation noise was smoothened with the Kalman filter and the needle localization algorithm was accelerated using bin packing method [10]. Also, the needle axis and its tip were localized in real-time.

In the literature provided above, most of the needle tip tracking methods are based on the Kalman filter [5], [6]. Needle tip tracking with the Kalman filter is a point based tracking method. Once the needle tip localization algorithms are executed, the Kalman filter tracks the needle tip using the localized needle tip points. Any other information from the US image is not used for tracking. During real-time needle tracking, the needle localization algorithm can fail, or misalignment can occur between the US image plane and the needle. In these instances, the Kalman filter cannot track the needle tip accurately [10].

Due to these shortcomings in the needle tip tracking methods, a visual tracking method for the needle tip is proposed. The main difference between the proposed visual tracking of the needle tip and other tracking methods is that the needle tip is detected once, and then the tip is tracked using the template needle images in the consecutive frames. Also, the templates are dynamically updated so that the needle tip tracking becomes invariant to intensity changes in the needle tip. As a result, the needle tip is tracked without using any needle localization algorithm, therefore tracking becomes more robust.

This paper introduces a visual tracking method for the needle tip in both lateral and transverse 2D US images. Second order optimization of sum of squared differences and sum of conditional variances are used for needle tip tracking. A template update strategy is used to prevent tracking failures caused by the template loss. The misalignment between US probe and the needle is detected by normalized cross correlation. In the experiments, a 2D US probe is mounted on a robotic arm and the needle tip is kept in the US image plane by the robot.

II. NEEDLE TIP TRACKING

Visual tracking method is an image registration between the current, $I(\mathbf{w}(\mathbf{x}; \mathbf{p}))$, and the template, $T(\mathbf{x})$ images. The \mathbf{x} vector, which contains image pixel coordinates, $\mathbf{x} = (x, y)$, are transformed by the warp model, $\mathbf{w}(\mathbf{x}; \mathbf{p})$. The aim of the image registration is to find the motion parameters, \mathbf{p} , which minimize the difference or maximize the similarity between the two images. The registration can be divided into two stages. In the first stage, similarity between an image pair is measured. In the second stage, parameters, \mathbf{p} , between the current image, $I(\mathbf{w}(\mathbf{x}; \mathbf{p}))$, and the template image, $T(\mathbf{x})$ are calculated using optimization techniques.

In order to measure the similarities between two images, sum of squared differences (SSD) [11], sum of conditional variances (SCV) [12], and normalized cross correlation (NCC) [13] functions can be used. SSD is the most commonly used similarity function. It can be easily implemented and run on a CPU. However, it is very sensitive to intensity changes. Due to the shortcomings of SSD, SCV is proposed [12]. SCV is very similar to SSD, but it is more robust to intensity changes. Similar to SCV, NCC is robust to intensity changes and it is a simpler method to measure similarity between two images.

The cost of these similarity functions are evaluated using a reference US image, which contains a needle structure (see Fig. 1-(a)). The template US image is cropped from the reference image (see Fig.1-(b)). The size of template image is 61×61 . Also, a second template image is created by changing pixel intensities of the needle pixels in Fig.1-(a) (see Fig.1-(d)). In the second template, the needle pixel intensities are very close to background. The template images are translated from -20 to 20 pixels with 1 pixel increments from the center of reference in x - and y -directions and similarities between the templates and the reference images are calculated. The results are shown in Fig. 1. As seen from the plots, the similarity reaches the minimum for the SSD and the SCV functions, whereas it reaches the maximum for the NCC functions, in the center.

$$\mathbf{w}(\mathbf{x}; \mathbf{p}) = \begin{bmatrix} (1 + p_1) \cdot x & + & p_3 \cdot y & + & p_5 \\ p_2 \cdot x & + & (1 + p_4) \cdot y & + & p_6 \end{bmatrix} \quad (1)$$

In this study, the needle tip is visually tracked using the SSD and the SCV. In order to find the parameters, \mathbf{p} , which minimizes the SSD or the SCV values, a second order Gauss-Newton optimization algorithm is used. In our experiments, the motion of the needle tip is pure translation in both transverse and lateral 2D US frames. Hence, an affine warp model is used (1), and parameters $\mathbf{p} = (p_1, p_2, p_3, p_4, p_5, p_6)$ are calculated. In the following chapters, SSD and SCV based visual tracking will be explained detailly.

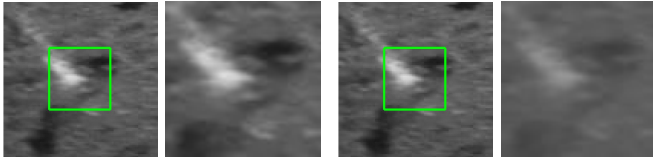
A. Visual Tracking using SSD

In this section, we describe the first and second optimization methods of SSD for image registration. SSD between $I(\mathbf{w}(\mathbf{x}; \mathbf{p}))$ and $T(\mathbf{x})$ can be computed as:

$$SSD(\mathbf{p}) = \sum_{\mathbf{x}} (I(\mathbf{w}(\mathbf{x}; \mathbf{p})) - T(\mathbf{x}))^2 \quad (2)$$

$I(\mathbf{w}(\mathbf{x}; \mathbf{p}))$ and $T(\mathbf{x})$ contains the intensity values of N pixels in the the current and reference images, respectively. Parameters, \mathbf{p} , which minimizes the similarity values between $I(\mathbf{w}(\mathbf{x}; \mathbf{p}))$ and $T(\mathbf{x})$ are calculated using optimization methods. For this purpose, $I(\mathbf{w}(\mathbf{x}; \mathbf{p}))$ and $T(\mathbf{x})$ are rewritten in the rectified vector format as:

$$I(\mathbf{w}(\mathbf{x}; \mathbf{p})) = \begin{bmatrix} I(\mathbf{w}(\mathbf{x}_1; \mathbf{p})) \\ I(\mathbf{w}(\mathbf{x}_2; \mathbf{p})) \\ \vdots \\ I(\mathbf{w}(\mathbf{x}_N; \mathbf{p})) \end{bmatrix}, \quad T(\mathbf{x}) = \begin{bmatrix} T(\mathbf{x}_1) \\ T(\mathbf{x}_2) \\ \vdots \\ T(\mathbf{x}_N) \end{bmatrix}$$



(a) Ref. Image (b) 1st Template (c) Ref. Image (d) 2nd Template

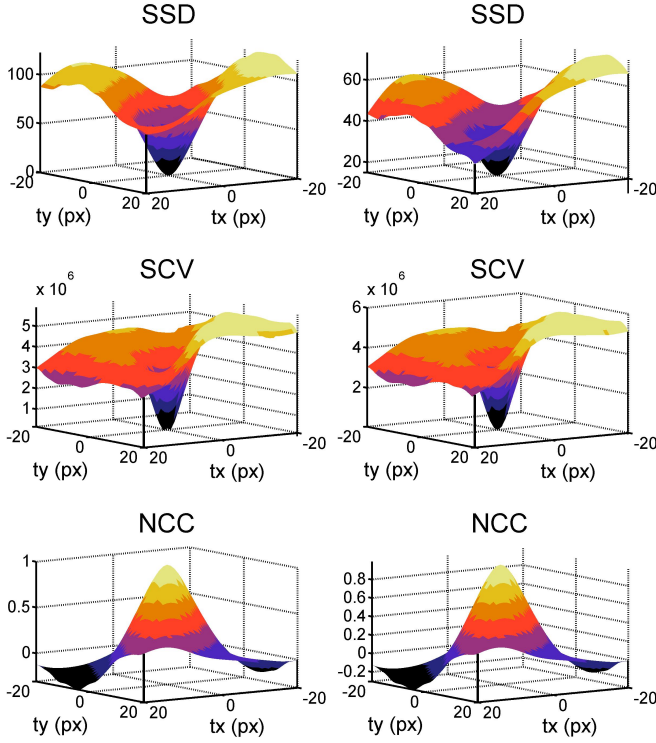


Fig. 1: 3D plots of SSD, SCV, and NCC values with respect to translations between two images. The left column contains similarity plots between (a) Reference image and (b) 1st template image. The right column contains the similarity plots between (c) Reference image and (d) 2nd template image.

In order to determine \mathbf{p} , firstly Taylor series expansion of $I(\mathbf{w}(\mathbf{x}; \mathbf{p}))$ is performed:

$$I(\mathbf{w}(\mathbf{x}; \mathbf{p} + \Delta \mathbf{p})) \approx I(\mathbf{w}(\mathbf{x}; \mathbf{p})) + \frac{\partial I(\mathbf{w}(\mathbf{x}; \mathbf{p}))}{\partial \mathbf{p}} \Delta \mathbf{p} + \frac{1}{2} \frac{\partial^2 I(\mathbf{w}(\mathbf{x}; \mathbf{p}))}{\partial \mathbf{p}^2} \Delta \mathbf{p}^2 + HOT \quad (3)$$

The equation above works for multiple dimensions ($I : \mathbf{R}^n \mapsto \mathbf{R}$). In that case, the first and second derivatives can be replaced with Jacobian ($J(\mathbf{p})$) and Hessian ($H(\mathbf{p}, \Delta \mathbf{p})$) matrices of $I(\mathbf{w}(\mathbf{x}; \mathbf{p}))$, respectively.

$$J(\mathbf{p}) = \frac{\partial I(\mathbf{w}(\mathbf{x}; \mathbf{p}))}{\partial \mathbf{p}}, \quad H(\mathbf{p}, \Delta \mathbf{p}) = \frac{\partial^2 I(\mathbf{w}(\mathbf{x}; \mathbf{p}))}{\partial \mathbf{p}^2} \quad (4)$$

Using (4), the Taylor series expansion of $I(\mathbf{w}(\mathbf{x}; \mathbf{p}))$ can be rewritten as:

$$T(\mathbf{x}) = I(\mathbf{w}(\mathbf{x}; \mathbf{p})) + J(\mathbf{p})\Delta \mathbf{p} + H(\mathbf{p}, \Delta \mathbf{p})\Delta \mathbf{p}^2 \quad (5)$$

By ignoring the $H(\mathbf{p}, \Delta \mathbf{p})\Delta \mathbf{p}^2$, the motion parameters can be estimated as follows:

$$\Delta \mathbf{p} = -(J(\mathbf{p}))^\dagger (I(\mathbf{w}(\mathbf{x}; \mathbf{p})) - T(\mathbf{x})) \quad (6)$$

where $()^\dagger$ is the pseudo-inverse of the matrix. Equation (6) estimates the motion parameters using first order optimization [14]. However, second order optimization of SSD converges faster and is more robust to noise. Also, it can be easily calculated by estimating $H(\mathbf{p}, \Delta \mathbf{p})$ as [12]:

$$H(\mathbf{p}, \Delta \mathbf{p}) \approx J(\mathbf{p}) - J(\mathbf{p}_0) \quad (7)$$

where $J(\mathbf{p}_0)$ is the Jacobian matrix of $T(\mathbf{x})$. By rewriting (5) using (7), $\Delta \mathbf{p}$ can be computed with second order optimization as follows:

$$\Delta \mathbf{p} = -2(J(\mathbf{p}) + J(\mathbf{p}_0))^\dagger (I(\mathbf{w}(\mathbf{x}; \mathbf{p})) - T(\mathbf{x})) \quad (8)$$

$J(\mathbf{p})$ and $J(\mathbf{p}_0)$ are computed as follow:

$$J(\mathbf{p}) = \nabla I \frac{\partial \mathbf{w}(\mathbf{x}; \mathbf{p})}{\partial \mathbf{p}}, \quad J(\mathbf{p}_0) = \nabla T \frac{\partial \mathbf{w}(\mathbf{x}; \mathbf{p})}{\partial \mathbf{p}}$$

where

$$\frac{\partial \mathbf{w}(\mathbf{x}; \mathbf{p})}{\partial \mathbf{p}} = \begin{bmatrix} x & 0 & y & 0 & 1 & 0 \\ 0 & x & 0 & y & 0 & 1 \end{bmatrix}$$

and ∇I , ∇T are the gradient of $I(\mathbf{w}(\mathbf{x}; \mathbf{p}))$ and $T(\mathbf{x})$, respectively.

Parameters, \mathbf{p} , are iteratively obtained by accumulating $\Delta \mathbf{p}$ in each iteration. Before the iteration loop starts, $J(\mathbf{p}_0)$ is computed and then $\Delta \mathbf{p}$ is computed in each iteration using (8). The iterations last until $\Delta \mathbf{p}$ is smaller than the threshold value, ϵ , or the predefined maximum iteration number is reached.

B. Visual Tracking using SCV

The needle tip can be tracked using the SSD. However, US images are inherently noisy and abrupt changes might occur in the needle pixels. The SSD is sensitive to these situations. In order to overcome the shortcomings of the SSD, the SCV is proposed to measure the similarity between the two images. The main difference between the two similarity measures is that the SCV adapts the template image using the current and the template images. Hence, the template image becomes invariant to sudden changes in the current image and tracking becomes more robust. The adaptive template, $\hat{T}(\mathbf{x})$, can be defines as:

$$\hat{T}(\mathbf{x}) = \mathcal{E}(I(\mathbf{w}(\mathbf{x}; \mathbf{p})) | T(\mathbf{x}))$$

where $\mathcal{E}(\cdot)$ is the expectation operator. $\hat{T}(\mathbf{x})$ can be calculated with the three consecutive stages [12]. In the first stage, joint probability (P_{IT}) between $I(\mathbf{w}(\mathbf{x}; \mathbf{p}))$ and $T(\mathbf{x})$ is calculated as:

$$P_{IT}(i, j) = \frac{1}{N} \sum_{\mathbf{x}} \delta(I(\mathbf{w}(\mathbf{x}; \mathbf{p})) - i) \delta(T(\mathbf{x}) - j) \quad (9)$$

where i and j are the intensity values in the $I(\mathbf{w}(\mathbf{x}; \mathbf{p}))$ and $T(\mathbf{x})$ images. N is the total number of pixels in the $I(\mathbf{w}(\mathbf{x}; \mathbf{p}))$ or $T(\mathbf{x})$, and $\delta(a)$ is the dirac delta function. In the second

stage, the marginal distribution of $T(\mathbf{x})$; P_T , is calculated using obtained the joint probability values in (10).

$$P_T(j) = \sum_i P_{IT}(i, j) \quad (10)$$

At the final stage, the expected grey levels in \hat{T} are calculated:

$$\hat{T}(j) = \sum_i i \frac{P_{IT}(i, j)}{P_T(j)}$$

After, the intensity values of image \hat{T} are calculated, SCV value between $I(\mathbf{w}(\mathbf{x}; \mathbf{p}))$ and $\hat{T}(\mathbf{x})$ can be computed as:

$$SCV(\mathbf{p}) = \sum_{\mathbf{x}} (I(\mathbf{w}(\mathbf{x}; \mathbf{p})) - \hat{T}(\mathbf{x}))^2 \quad (11)$$

As seen in (11), the SCV and the SSD values between two images are computed in the same way. Therefore, \mathbf{p} which minimizes the SCV value between $I(\mathbf{w}(\mathbf{x}; \mathbf{p}))$ and $\hat{T}(\mathbf{x})$ can be calculated with a second order optimization of the SSD equation (8). The optimization equation can be rewritten as:

$$\Delta \mathbf{p} = -2(J(\mathbf{p}_{\hat{T}}) + J(\mathbf{p}))^\dagger (I(\mathbf{w}(\mathbf{x}; \mathbf{p})) - \hat{T}(\mathbf{x})) \quad (12)$$

where $J(\mathbf{p}_{\hat{T}})$ is the Jacobian of the $\hat{T}(\mathbf{x})$, which can be computed with the gradient of \hat{T} as:

$$J(\mathbf{p}_{\hat{T}}) = \nabla \hat{T} \frac{\partial \mathbf{w}(\mathbf{x}; \mathbf{p})}{\partial \mathbf{p}}$$

During the tracking, \hat{T} is computed once with a new frame, before the iteration loop starts. Then \mathbf{p} is iteratively calculated using (12) until the desired values are reached.

III. TEMPLATE UPDATE STRATEGY

In this section, the needle template update strategy is described. It is one of the significant steps of the needle tip tracking. If the needle template is not updated correctly, the needle tip is lost and the tracking fails. In order to update the needle template correctly, three commonly used strategies are evaluated below.

Strategy 1: No Update. The template is not updated during the tracking ($T_{n+1}(\mathbf{x}) = T_1(\mathbf{x})$). However, this strategy is not suitable for needle tip tracking because the appearance of the needle shape changes during the needle insertion. Also, sudden changes in the needle pixels' intensities might occur due to misalignment between the needle and the US probe. Due to these shortcomings, the template image must be updated in every frame.

Strategy 2: Naive Update. The template is updated in every frame ($T_{n+1}(\mathbf{x}) = T_n(\mathbf{x})$). Hence, the template becomes invariant to appearance changes during the tracking. After \mathbf{p} is calculated between two images, there is a residue error between template and current images. This error is accumulated during the tracking and template is drifting along motion direction. Eventually, needle tip tracking fails. Similar to Strategy 1, Strategy 2 is not suitable for needle tip tracking because the template is drifting. Therefore, the drift must be corrected to prevent failures during the tracking.

Strategy 3: Template Update with Drift Correction. In this Strategy, template is updated in every frame like Strategy 2. But, new template is then registered with the first template of the needle [15]. Hence, the residue error due to image registration between the template and the current images is so minimized that the drift is corrected. This method improves the tracking accuracy significantly and prevents tracking failure. Also, it is a simple method and can be easily implemented. All of the Strategies are compared using 2D US frames while the needle is inserted into agar-gelatin based phantom with a needle insertion robot. The outputs of the Strategies are shown in Fig. 2. The result of the visual tracking of needles in 2D lateral and transverse images are shown in Fig. 3 and Fig. 4, respectively.

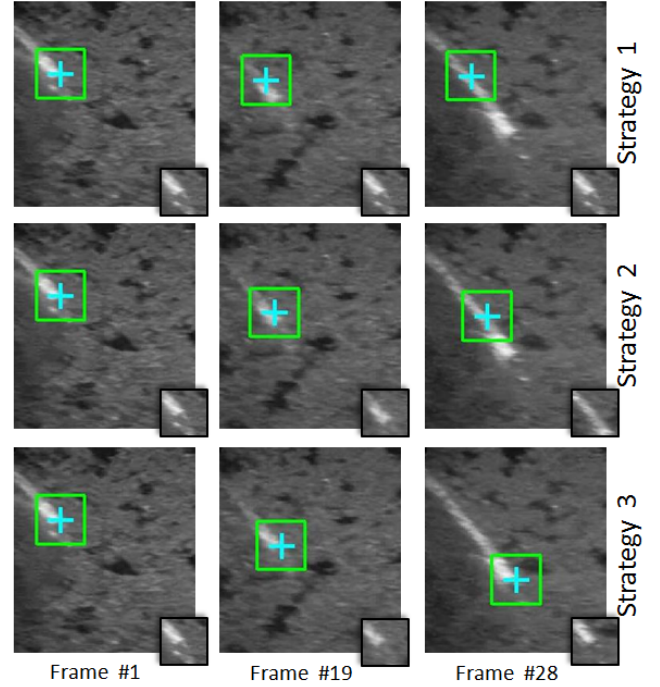


Fig. 2: Comparison of the template update strategies. **Strategy 1:** No update. **Strategy 2:** Template updated in each frame. **Strategy 3:** Template update with drift correction.

IV. NEEDLE LOSS DETECTION & RECOVERY

While inserting the needle, there can be misalignment between the US image plane and the needle. In this case, the needle would be out of the US image plane, therefore the needle will be lost in the image. During the needle tip tracking, the needle template is updated in each frame and then the drift is corrected (Strategy 3). If the needle tip loss is not detected, template will be still updated, and the updated template won't contain any needle structure. Eventually, tracking would fail.

In order to prevent tracking failures, the target loss must be detected. For this purpose, similarity between current template image ($T_n(\mathbf{x})$) and image obtained after the tracking ($T_{n+1}(\mathbf{x})$) can be used. In our experiments, SSD, SCV, and

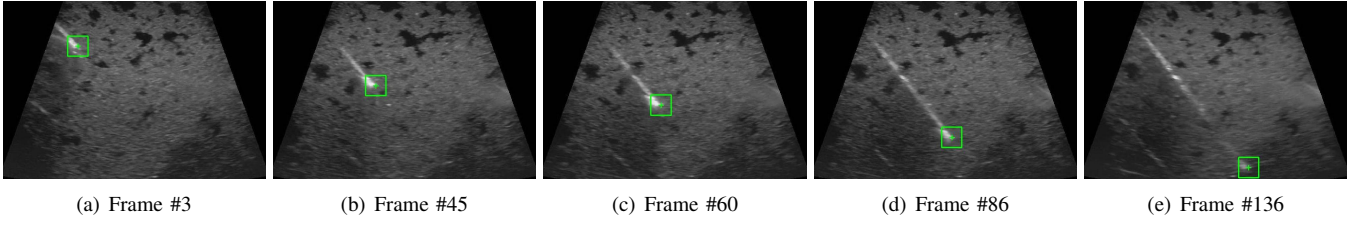


Fig. 3: Results using visual tracking of the needle tip in 2D lateral US images.

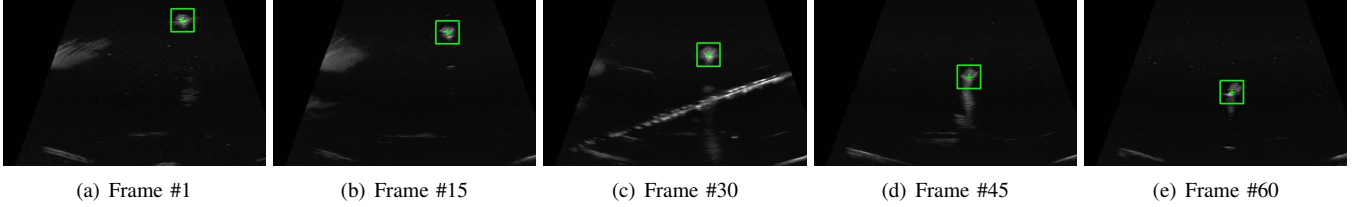


Fig. 4: Results using visual tracking of the needle tip in 2D transverse US images.

NCC are evaluated. However, values of the SSD, and the SCV are not normalized and also thresholding values for detecting the target loss using these measures vary by each image. On the other hand, the NCC value is normalized. Its value changes between -1 and 1. If the NCC value is 1, images are identical, whereas if the NCC value is -1, images are completely irrelevant. Also, this is a robust similarity measure (see Fig. 1). The NCC value between $T_n(\mathbf{x})$ and $T_{n+1}(\mathbf{x})$ is computed as:

$$NCC = \frac{\sum_{\mathbf{x}} (T_{n+1}(\mathbf{x}) - \bar{T}_{n+1}) \cdot (T_n(\mathbf{x}) - \bar{T}_n)}{\sqrt{\sum_{\mathbf{x}} (T_{n+1}(\mathbf{x}) - \bar{T}_{n+1})^2} \cdot \sqrt{\sum_{\mathbf{x}} (T_n(\mathbf{x}) - \bar{T}_n)^2}}$$

where \bar{T}_{n+1} and \bar{T}_n are the mean intensity values of $T_{n+1}(\mathbf{x})$ and $T_n(\mathbf{x})$, respectively.

In our experiments, we observed that if the needle is in the US image plane, the NCC value is very close to 1. In contrast, if the needle is lost in the image plane, the NCC value drops significantly (see Fig. 6). During the needle tracking, 0.8 is determined as threshold value for detecting the target loss. If the needle loss is detected once, the needle insertion is stopped, and the current template is not updated, which means that the last appearance of the needle is kept. Then, the needle is sought by the US probe around the last detected needle location. This process is applied to each frame until NCC value reach the 0.75. If the NCC value reaches 0.75, this means that the needle is recovered in the image, and the needle tracking starts again. An example output of the needle loss and recovery is shown in Fig. 5. The NCC values versus the frame numbers are plotted in Fig. 6.

As seen in Fig. 5-(c), after the needle is lost in the image, there can be needle like structures in the image. If the needle localization algorithm is applied, these structures would probably be falsely detected as the needle. Hence, the needle tip tracking would fail. With the proposed needle target recovery method, the needle tip is localized without using

any localization algorithm and the needle tip is correctly recovered using the whole US image.

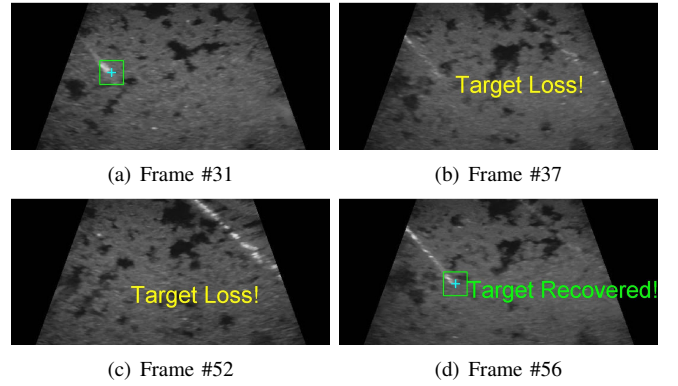


Fig. 5: Result of the needle loss detection & recovery. (a) The needle tip is being visually tracked and the needle is in the image plane. (b)-(c) The needle tip is out of the US image and needle loss is detected. (d) The needle tip is again in the US image plane and the needle tip is detected using the last template image of the needle before it got lost.

V. EXPERIMENTS

A. Experimental Setup

In the experiments, a GE LOGIQ P5 2D US machine and a GE 11L linear 2D US probe were used to acquire images. To capture the images from the US machine, EURESYS PICOLO HD 3G frame grabber was used. Experiments were carried on gelatin and agar mixture, agar-based and gelatin-based phantoms, ethanol and distilled water mixture, and distilled water. Phantoms were prepared using the recipes given in [9]. 22G×15 cm biopsy needles and 12G×26 cm stainless steel shafts were used in the experiments.

The US probe was attached to a 6-DOF industrial robot arm (KUKA KR 6 R9000 sixx), and the arm was manipulated to keep the needle tip in the 2D US image plane. A

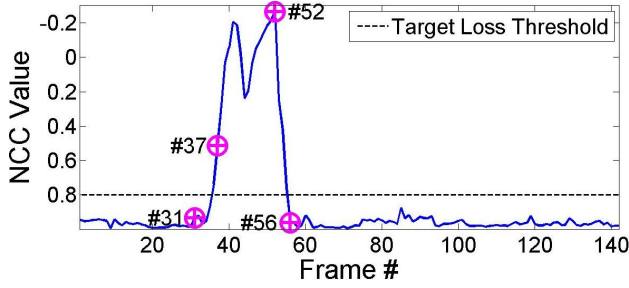


Fig. 6: NCC value versus frame number. The NCC value of each frame illustrated in Fig. 5 is marked with \oplus and the corresponding frame number is indicated.

needle insertion robot was used to insert the biopsy needles during the experiments. The insertion robot has 5-DOF and designed to conduct percutaneous biopsies on humans. The experimental setup is shown in Fig. 7.

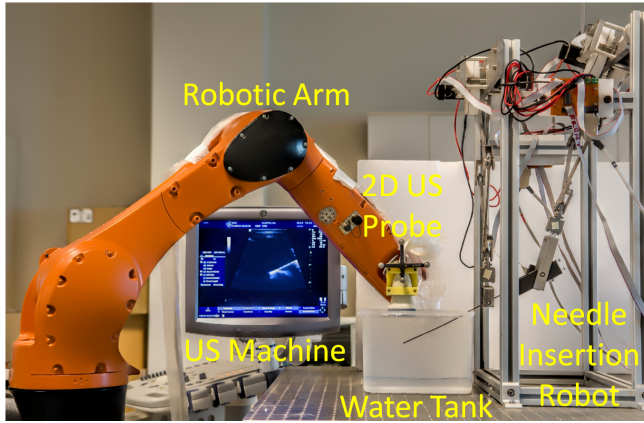


Fig. 7: Experimental setup: Robotic arm holds the US probe and needle robot is inserting the needle into the water tank.

B. Experimental Results

In the experiments, the needles were inserted both manually and using needle insertion robot into phantoms and they were imaged both in 2D lateral and transverse US images. In the robotic insertions, US probe and the needles were aligned and the needle tip was kept in the US image plane using robotic arm. During the robotic insertions, the velocity of needle was set to 10 mm/s.

In the needle insertion experiments, 16 lateral and 4 transverse frame sequences were acquired. The total number of frames was 7074 and the size of the frames was 640×480 pixels. Acquired frames during the needle insertion contain needle loss and abrupt intensity changes in the needle pixels. Heterogenous phantoms especially fabricated to show the needle can be visually tracked in various type of backgrounds. During the needle insertions, the needle tip was tracked successfully in all of the frame sequences. In the misalignment cases, the needle tip disappeared in the image plane. After the needle tip was aligned with US probe, the needle tip was detected without using any needle tip localization algorithm. In addition, template drifting in frame

sequences was corrected with template update Strategy 3 so that the tracking did not fail.

The algorithm was implemented in MATLAB and ran on 64-bit Windows 7 workstation, which has an Intel Xeon E5-2620 CPU running at 2 GHz and 32 GB RAM. During the tracking, the size of the template images was 20×20 . The maximum iteration number and threshold value (ϵ) for breaking the iteration loop were set to 50 and 0.01, respectively. The execution times are tabulated in Table I. The processing time was reduced over 40% in both tracking methods using 2^{nd} order optimization.

TABLE I: Execution time for the methods used

Method	Execution Time [s]	
	1 st order optimization	2 nd order optimization
SSD	0.18 ± 0.13	0.10 ± 0.04
SCV	0.24 ± 0.09	0.14 ± 0.02

REFERENCES

- [1] H. Sen, M. A. Bell, Y. Zhang, K. Ding, J. Wong, I. Iordachita, and P. Kazanzides, "System integration and preliminary in-vivo experiments of a robot for ultrasound guidance and monitoring during radiotherapy," in *Advanced Robotics (ICAR), 2015 International Conference on*, July 2015, pp. 53–59.
- [2] Y. Zhao, A. Bernard, C. Cachard, and H. Liebgott, "Biopsy needle localization and tracking using roi-rk method," in *Abstract and Applied Analysis*, vol. 2014. Hindawi Publishing Corporation, 2014.
- [3] P. M. Novotny, J. A. Stoll, N. V. Vasilyev, P. J. del Nido, P. E. Dupont, and R. D. Howe, "Gpu based real-time instrument tracking with three dimensional ultrasound," in *Proceedings of the 9th international conference on Medical Image Computing and Computer-Assisted Intervention - Volume Part I*, 2006, pp. 58–65.
- [4] T. K. Adebar and A. M. Okamura, "3d segmentation of curved needles using doppler ultrasound and vibration," in *Information Processing in Computer-Assisted Interventions*. Springer, 2013, pp. 61–70.
- [5] G. Vrooijink, M. Abayazid, and S. Misra, "Real-time three-dimensional flexible needle tracking using two-dimensional ultrasound," in *Proceedings of the IEEE International Conference on Robotics and Automation (ICRA)*, no. 2, May 2013, pp. 1680–1685.
- [6] P. Chatelain, A. Krupa, and M. Marchal, "Real-time needle detection and tracking using a visually served 3D ultrasound probe," in *Proceedings of the IEEE International Conference on Robotics and Automation (ICRA)*, no. 2, May 2013, pp. 1668–1673.
- [7] P. Chatelain, A. Krupa, and N. Navab, "3d ultrasound-guided robotic steering of a flexible needle via visual servoing," in *IEEE Int. Conf. on Robotics and Automation, ICRA'15*.
- [8] M. Kaya and O. Bebek, "Needle localization using gabor filtering in 2D ultrasound images," in *Proceedings of the IEEE International Conference on Robotics and Automation (ICRA)*, May 2014.
- [9] —, "Gabor filter based localization of needles in ultrasound guided robotic interventions," in *IEEE International Conference on Imaging Systems and Techniques (IST)*, October 2014.
- [10] M. Kaya, E. Senel, A. Ahmad, O. Orhan, and O. Bebek, "Real-time needle tip localization in 2D ultrasound images for robotic biopsies," in *IEEE International Conference on Advanced Robotics (ICAR)*, 2015.
- [11] S. Baker and I. Matthews, "Lucas-kanade 20 years on: A unifying framework," *International journal of computer vision*, 2004.
- [12] R. Richa, R. Sznitman, R. Taylor, and G. Hager, "Visual tracking using the sum of conditional variance," in *Intelligent Robots and Systems (IROS), 2011 IEEE/RSJ International Conference On*, 2011.
- [13] G. G. Scandaroli, M. Meilland, and R. Richa, "Improving ncc-based direct visual tracking," in *Computer Vision—ECCV*. Springer, 2012.
- [14] G. D. Hager and P. N. Belhumeur, "Efficient region tracking with parametric models of geometry and illumination," *Pattern Analysis and Machine Intelligence, IEEE Transactions on*, 1998.
- [15] I. Matthews, T. Ishikawa, and S. Baker, "The template update problem," *IEEE Transactions on Pattern Analysis & Machine Intelligence*, 2004.